Characterization of IASCC crack tips extracted from neutron-irradiated flux thimble tube specimens in view of a probabilistic fracture model

Characterization of IASCC crack tips extracted from neutron-irradiated flux thimble tube specimens in view of a probabilistic fracture model

A. G. Penders[a,b,1,2,3,*], M. J. Konstantinović[a,1], W. Van Renterghem[a,1], R-W. Bosch[a,1], D. Schryvers[b,2,3], F. Somville[c,4]

[a] *SCKCEN, Boeretang 200, B-2400 Mol, Belgium*

[b] *EMAT, University of Antwerp, Groenenborgerlaan 171, 2020 Antwerp, Belgium*

[c] *ENGIE-Tractebel, Boulevard Simon Bolivar 34-36, 1000 Brussels, Belgium*

Abstract

This study reports the properties of irradiation assisted stress corrosion crack tips extracted by means of focused-ion beam from 60-80 dpa neutron-irradiated O-ring specimens tested under straining conditions under a pressurized-water reactor environment. Various crack tip morphologies and surrounding deformation features were analyzed as a function of applied stress, surface oxidation state and loading form - constant versus cyclic. All investigated cracks exhibit grain boundary oxidation in front of the crack tip, with the extent of oxidation being proportional to applied stress. These findings clearly demonstrate that, under the subcritical crack propagation regime, the grain boundary oxide grows faster than the crack. On the other hand, crack tips appertaining to specimens with removed oxide layer at the outer surface show comparatively less oxidation at the crack tip, which could indicate towards crack initiation from regions that exemplify lower stress, such as the O-ring inner surface. Cyclic loading is found to have a more pronounced effect on the crack tip microstructure, demonstrating increased deformation twinning and α'-martensitic transformation, which signifies towards an increased susceptibility to intergranular failure. Still, the extent of crack tip grain boundary oxidation in this case agrees well with expected values for maximum stress applied during cyclic loading. All results are interpreted based on the probabilistic subcritical crack propagation mechanism and provide strong support to a stress-driven internal oxidation model.

Keywords: IASCC, 316L, neutron-irradiation, flux thimble tube, (S)TEM, FIB, internal oxidation,

*Corresponding author

Email addresses: apenders@sckcen.be (A. G. Penders), mkonstan@sckcen.be (M. J. Konstantinović), wvrenter@sckcen.be (W. Van Renterghem), rbosch@sckcen.be (R-W. Bosch), nick.schryvers@uantwerpen.be (D. Schryvers)

URL: https://www.sckcen.be/ (A. G. Penders), https://www.uantwerpen.be/en/research-groups/emat/ (A. G. Penders)

[1] Studiecentrum voor Kernenergie - Centre d'Etude l'Energie Nucléaire (SCKCEN)

[2] Electron Microscopy for Materials Science - EMAT

[3] University of Antwerp

[4] ENGIE-Tractebel

1. Introduction

Despite for their desirable strength, fracture toughness, and general resistance to corrosion, austenitic stainless steels used for structural materials in nuclear power plants (NPPs) experience property changes as a consequence of complex material degradation phenomena [1, 2, 3, 4, 5]. These changes can bring about intergranular component failures in the form of irradiation-assisted stress corrosion cracking (IASCC) [6, 7, 8, 9, 10]. Prime examples of IASCC cracking entail the sudden intergranular failures of baffle-to-former bolts [11], first observed in French pressurized-water reactors (PWR). Due to the lack in failure predictability, these observations have raised concerns on the material reliability, especially in the light of potential NPP operation extensions. Influential factors to consider are the high degrees of material stresses and the exposure time to the NPP high-temperature water environment. Additional elements that dominate the material's lifetime include some degree of non-monotonic loading conditions caused by the variability in thermal transients and loading-unloading cycles [12, 13, 14]. Despite current best efforts, no single indicative failure mechanism for IASCC has been yet agreed upon. Predictive methodologies instead incorporate the many different interdependencies between the correlating factors related to IASCC, in an attempt to improve current mitigation strategies.

One of the prime mechanical ways to investigate IASCC contributing factors is on the basis of constant load compression tests. In this regard, over 80 neutron-irradiated O-ring specimens were cut from a 316L stainless steel (SS316L) flux thimble tube redeemed from the commercial Tihange PWR in Belgium. These O-ring specimens were subjected to load compression tests in order to investigate IASCC crack initiation in terms of time-to-failure (TTF) [15]. Experimental results showed a large intrinsic scatter for O-rings tested under similar conditions, the origin of this scatter remained not fully understood. For instance, under an applied stress of 55% of the irradiated yield stress, the failure time ranged between 100 h to 2000 h. Recent rendition of these failures by Konstantinović [16], one of the authors of this study, indicated that the scatter may be correlated with the parameters governing the crack initiation solely in the oxidized part of the stainless steels. Following the concept of internal oxidation [17, 18], intergranular oxides are thought to be responsible for the embrittlement and the lowering of fracture resistance as a consequence of oxide diffusion leading into the crack tip grain boundary. If the cracking is entirely dictated by the failure of the oxide, it is reasonable in that sense to consider a probabilistic oxide strength in order to determine the cracking probability. In this regard, Konstantinović [16] developed a probabilistic fracture model on the grounds of the statistical Weibull treatment of oxide strength and described the subsequent growth of cracking in terms of a subcritical crack propagation (SCP) process. Through the idea of the weakest link theory, failure at any point in time is governed by certain distribution of flaws or initiation points within the oxide. These flaws correlate with a weaker probabilistic oxide strength which may result in a higher probability of failure, especially in more voluminous oxides where possibility of inherent flaws is far greater.

Despite being listed amongst the leading intergranular degradation mechanisms under PWR environments, the internal oxidation concept [17, 18] is not without dispute, especially not when it comes to the cracking in stainless steels [19]. Experimental investigations of active cracks should confirm the presence of brittle intergranular oxides ahead of propagating crack tips. Moreover, it should be established that, at all times, the intergranular oxides grow faster than the propagation rate of the crack itself. Considering specifically the case of SCC without the aspect of irradiation, no experimental verification in support of these reasonings has been presented so far. However, in regards to irradiated steels, our previous investigation regarding the examination of IASCC tips did show brittle propagation of cracks within leading oxidized grain boundaries [20]. Arguably, the as-irradiated microstructure not only enhances the dislocation density but also affects the leading grain boundary chemistry through processes like radiation-induced segregation (RIS). These effects may accelerate the oxidation kinetics in such a way that justifies reasonings for internal oxidation of leading grain boundary structures in irradiated steels. The brittle oxide cracking was found to be associated with multiscale fracture bands in the porous regions of the intergranular oxide. When these oxides are subjected to tensile stress, the cracking susceptibility of the oxides is promoted through embrittlement of the surrounding metallic matrix. Specifically for the cracks appertaining to a specimen tested at a relatively low stress intensity (390 MPa), coalescence of such fracture bands at the oxidized crack tip led to further cracking of the leading grain boundary. Moreover, our results indicated that the cracking is facilitated in the cleavage stress direction, whereat the grain boundary normal is aligned in parallel with the acting stress orientation. Extensive deformation structures in the form of twins and deformation bands were observed at and around the cracks, in addition to what appeared as martensitic laths following the Kurdjumov-Sachs (K-S) [21] and Nishiyama-Wasserman (N-W) [22] orientation relationships [23]. Phase-transformed phases in addition to the nucleation of deformation twins may severely contribute to local strain-hardening by impeding the dislocation glide in close vicinity to the crack [24, 25, 26], which can in turn promote the susceptibility to cracking.

Validation of the internal oxidation based SCP mechanism for intergranular cracking of stainless steels requires distinct observations of IASCC cracks and crack tips formed under various applied stress and initial material surface state conditions. Both stress and surface oxidation are believed to play a crucial role for the initiation of intergranular cracks, in particular when the probabilistic nature of brittle oxide is considered. However, thus far, there is no systematic study of the effect of macroscopic stress on the internal oxidation of the crack tip. Therefore, this study presents a continuation of our previous work on the characterization of IASCC crack tips and testing [20], as part of SCKCEN's thimble tube corrosion framework [15, 16, 27, 28]. Focused-ion beam (FIB) is utilized to extract IASCC crack tips from highly irradiated SS316L O-ring specimens tested under: (i) increasing stress levels, (ii) different oxidized surface states, and (iii) cyclic loaded conditions. Subsequent transmission electron

microscopy (TEM) is employed to study the extent of intergranular cracking, its cracking morphology, and the surrounding deformation field. Microstructural analyses and investigations of the crack's deformation field are performed on a total of 24 cracks extracted from all presented O-rings and interpreted in relation to the acting stress intensity. The aim of this work is to correlate the different sample and loading conditions with the crack propagation mechanism. Results achieved within this study may facilitate in the development of predictive methodologies and mitigation strategies related to IASCC cracking.

2. Materials and methods

2.1. Load testing

A 316L cold-worked (20% CW level) stainless steel flux thimble tube originating from the commercial Belgian PWR NPP Tihange 2 was made available for the purpose of studying IASCC cracking. The material composition outlined in Tab. 1 is comparable to the ASTM 316L specification standards and to other flux thimble tube materials reported in the literature [29]. As described in references [15, 20], the thimble tube was cut along its length to produce numerous O-ring specimens with varying dose profiles. These O-rings were deburred to remove any preferential crack initiation sites and consequently subjected to mechanical load compression tests. Details on the test description may be found in the references accordingly.

Several O-ring specimens were compressed to failure by varying the applied stress levels, TTFs, surface and loading state during the mechanical testing. Three equivalent specimens were tested under constant load testing by increasing the stress, ranging from 390 to 690 MPa, well below the irradiated yield stress estimated to be about 1000 MPa. An additional sample was prepared with a different surface oxide state, in order to investigate its implication on the crack initiation within the surface oxide. The initial in-service native PWR oxide layer was abraded prior to the initiation of the constant load test by mechanical soft grinding. In this way, the metallic surface quickly establishes a non-native oxide layer, composed of an oxide that formed under aerated and under simulated PWR conditions during testing. Implication of the non-native oxide to the initiation of IASCC cracks and overall TTF of the O-ring specimen could indicate some of the prerequisites required for cracking and shed light on the cracking mechanisms itself. Lastly, a final fifth specimen was subjected to low-cycling fatigue testing instead of the conventional constant load tests performed in all other O-ring specimens. The loading cycle consisted of a triangular waveform with a transient time of about 60 minutes, wherein the compressive stresses are systematically cycled between 40 to 100 % of its maximum stress value, averaging around 70 % stress overall. An overview of the specimens retained for investigation within this study may be found in Tab. 2.

2.2. Sample preparation

Post load testing, the O-rings fractured into several interconnected pieces; one example for a typical O-ring is displayed in Fig. 1. A single piece that exhibit

Table 1: Chemical composition of Tihange thimble tube O-ring specimens made from 316L cold-worked (20% CW level) stainless steel.

	Fe	**Ni**	**Cr**	**Mo**	**S**	**P**	**Si**	**Mn**	**Co**	**C**
Comp (wt. %)	Bal.	12.8	17.0	2.68	0.009	0.022	0.53	1.79	0.07	0.044

Table 2: Overview of the autoclave loading conditions simulating IASCC crack initiation under PWR (2 ppm Li, 1000 ppm B, 30 cm^3/kg H_2, pH_T = 7.06 (calculated)) atmosphere conditions operating at 320 °C.

Specimen ID	**Length (mm)**	**Dose (dpa)**	**Stress (MPa)**	**No. fractured pieces**	**TTF (h)**	**Exposure time (h)**	**Surface condition**	**Loading path**
TTO-1-053	10.425	60	390	5	1910	4350	PWR oxide surface	Constant
TTO-1-071	8.32	80	500	4	190	350	PWR oxide surface	Constant
TTO-1-001	5.94	80	690	3	14.8	120	PWR oxide surface	Constant
TTO-1-090	5.89	80	700	5	155.2	1102	Non-native oxide surface	Constant
TTO-1-066	14.66	80	280 ± 120	4	1680	1680	PWR oxide surface	Cyclic

part of the primary fracture surface was retained for subsequent FIB analysis. Such pieces underwent a specific cutting procedure in order to reduce the sample's activity to accommodate it with the instrument's threshold values, see Fig. 1A. The remaining piece is a reduced section of the primary fracture surface wherein branched cracks are still clearly visible, see Fig. 1B. SEM investigation of this surface showed a predominant intergranular cracking behavior for each specimen, although some variation depending on the stress conditions was observed. While the primary fracture surface of low stressed samples indicated a fully intergranular surface [20], higher stressed samples definitely exhibited some transgranular cracking along its fracture surface. These results might indicate towards stress overload occurring specifically at higher imposed stress conditions. Intermediate stress-tested samples lie in between both extremes, only indicating minor signs of transgranular cracking along the primary fracture surfaces. Interestingly, along the cyclic loaded O-ring's outer surface, visible striation marks were observed in close vicinity of the main fracture which represent failure by material fatigue, see Fig. 1C. All specimens showed some variation in crack branching, propagating intergranularly across multiple grains overall.

2.3. FIB analysis of IASCC tips

Most cracks were extracted from the O-ring's primary fracture surface using the Thermo Scientific Scios DualBeam FIB-SEM according to the standard in-situ FIB lift-out technique, except for those appertaining to samples TTO-1-001 (690 MPa) and some cracks of TTO-1-066 (280 MPa - cyclic loading). Hard-lining restrictions on the sample's activity level and its size dimensions made it practically very difficult to tilt the primary fracture surface facing upwards towards the FIB's electron beam. Therefore, in reconciliation of this problem, it was opted to only extract cracks from TTO-1-001's and some of 066's outer fracture surface instead. The outer O-ring surface exposed to the PWR environmental conditions still showed intergranular cracks propagating in the

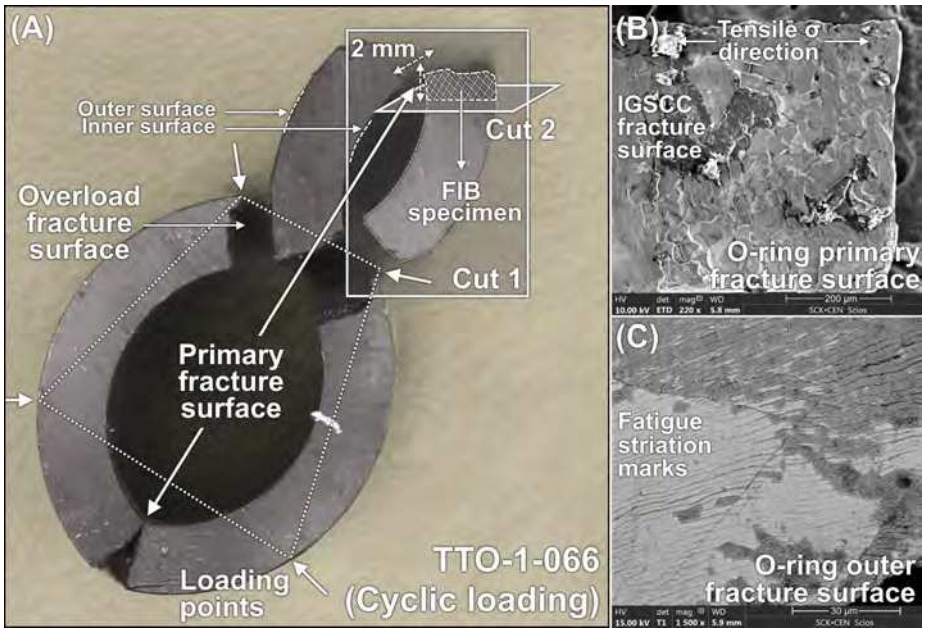

Figure 1: TTO-1-066 (280 MPa - cyclic loading) sample preparation. (A) O-ring post constant load compression testing. Indications of the loading points and transversal cut along the middle of the specimen are depicted. The second cut of the remaining piece is performed close to the primary fracture surface. (B) SEM image of the fracture surface illustrating a predominantly intergranular fracture surface appearance. (C) Backscattered SEM image of fatigue striation marks appearing along the O-ring's outer surface.

bulk, although not as extensively as observed from the primary fracture surface. The consequence of this sample orientation with respect to all other samples only relates to the direction of the tensile stress, which is further taken into account in regards to its angle with the crack tip orientation, see Tab. 3. However, FIB-extraction of IASCC crack tips from the primary fracture surface remained equally challenging, given the large branching nature of the cracks along multiple grains, especially for lower stress-tested specimens. Still, IASCC embedded cracks were managed to be extracted from both surfaces and ultimately thinned to electron-transparency levels using the standard FIB cross-sectional lift-out procedure described in our previous publication [20]. Crack curtaining i.e., favorable milling underneath the bulk embedded crack tips, remained a limiting factor when the lamellae achieved electron-transparency levels. Nevertheless, the curtaining was kept at a minimum using dedicated ion-beam conditions and ion-milling rates.

Table 3: Overview of FIB-prepared TEM-lamellae of extracted intergranular crack tips from the outer surface (OS) or main fracture surface (FS) of O-rings tested under varying conditions (θ: angle between crack propagation direction and tensile stress direction).

Specimen ID	**Lamella ID**	**Surface**	θ	**Remarks**
TTO-1-053 (390 MPa)	6 crack tips (see Penders et al. [20])			
TTO-1-071 (500 MPa)	L03	FS	74°	Fractured grain boundary tapering down towards shear crack tip; Branching at triple junction.
	L07	FS	47°	Similar as L03.
	L11	FS	2°	Similar as L03.
TTO-1-001 (690 MPa)	L05	OS	107°	Shallow cleavage crack extending from oxidized OS. No branching.
	L07	OS	95°	Cleavage crack tapering straight towards oxidized cleavage crack tip. No branching.
	L16	OS	4° & 131°	Wide cleavage crack arrested at oxidized triple junction; two crack tips in cleavage and shear directions. No branching.
	L23	OS	1° & 101°	Similar as L16.
TTO-1-090 (700 MPa - non-native oxide)	L01	FS	1°	Wide shear crack tapering down to oxidized shear crack tip. No branching.
	L06	FS	2°	Similar as L01.
	L07	FS	0°	Shear crack impeded by oxidized MnS particle. No branching.
	L08	FS	16°	Similar as L01.
TTO-1-066 (280 MPa - cyclic loading)	L02	OS	100°	Narrow cleavage crack tapering down to oxidized triple junction. No branching.
	L07	FS	16°	Narrow shear crack following curvature of grain boundary. Branching at triple junctions resulting in one extracted crack tip.
	L08	FS	4°	Similar as L07.
	L09	FS	20°	Similar as L07.

Tab. 3 presents a complete overview of all the cracks that were subsequently investigated using TEM analysis. A multitude of crack embedded lamellae were prepared for each individual specimen. Ultimately, a total of 24 fully developed crack tips were completely extracted. Typical crack morphologies that were either single tips that branched off from a fully oxidized grain boundary triple junction, or narrow intergranular cracks developing perpendicular from the lamella surface without showing any existential branching. It is apparent from the collected crack tips that the tensile stress plays an important role for crack initiation in all sets of specimens. First and foremost, it was observed that crack branching occurred more prominently at lower stress values than compared to

the otherwise straight developed crack morphology observed more frequently at higher stressed samples. This observation may be correlated with the imposed stress direction which is aligned in parallel for crack tips extracted from the O-ring's outer surface, while it acts in the in-plane direction into the bulk when facing the primary fracture surface. Therefore, cracks extracted in cross-sectional orientation from the outer surface initiate in cleavage-mode (mode I), while those extracted from the primary surface initiate in shearing-mode instead (mode II). The effective stress orientation at the crack tip naturally depends on the crack path along the leading grain boundary, though it was typically observed that cracks arrested whenever the tensile stress acted in shearing-mode at the propagating crack tip. Sheared cracks generally resulted in much shorter developed crack lengths, while cleavage propagating cracks generally extended much deeper within the bulk beyond the size that could be geometrically extracted with FIB. To that end, a much greater success rate was observed in extracting a shearing-mode crack tips, simply because the crack length was typically shallower.

2.4. (S)TEM analysis

Characterization of IASCC crack tips was mainly performed using a 300 kV JEOL 3010 scanning (S)TEM equipped with a LaB_6 electron gun filament and an Oxford Instrument EDS link spectrometer with corresponding Si(Li) detector. Conventional analyzes mainly consisted of selected area electron diffraction (SAED) bright (BF−) and centralized dark-field (DF−) TEM imaging operations. Fresnel underfocus contrast imaging was employed to reveal porous structures and salient fracture bands at the crack tip. High-resolution (HR-) TEM is used for the direct imaging of the interplanar spacings of crystalline materials at atomic resolution. Fast Fourier transformed (FFT) diffractograms can be obtained from HR-TEM imaged materials in order to obtain relevant crystallographic information. External TEM software such as CrystalDiffract®: a powder diffraction program from CrystalMaker Software Ltd, `http://www.crystalmaker.com`, was employed to simulate spot-like diffraction patterns in order to validate encountered crystal structures. Analytical characterization consisted of both TEM energy dispersive X-ray spectroscopy (EDS) and STEM techniques. EDS spot-analyzes were acquired at the smallest attainable spot size (estimated to be about 25 nm's) using the same JEOL 3010 scanning (S)TEM, while STEM was performed on an aberration-corrected X-FEG Thermo Fisher X-Ant-EM or a JEM-ARM300F Grand ARM at accelerating voltages of both 300 kV. STEM high-angle annular dark-field (HAADF) contrast imaging was predominantly used for the collection of line scans and spectral maps over IASCC crack tips and leading grain boundaries. Z-contrast imaging was employed to achieve image contrast that scales according to thickness and average atomic number ($I \propto Z^2$) of the specimen, thus providing local chemically-sensitive information of the region of interest.

3. Results

3.1. Microstructural characterization based on applied stress

3.1.1. Crack deformation field

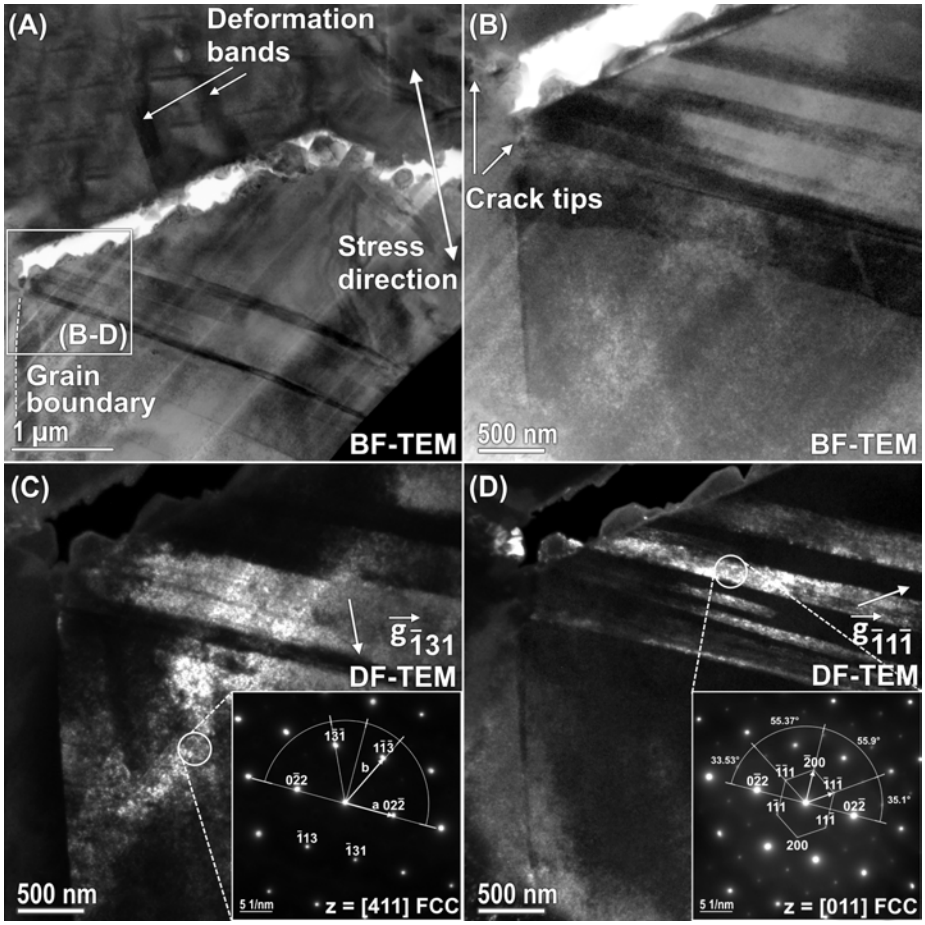

Figure 2: TTO-1-001 (690 MPa) L16 (A) Magnified BF-TEM overview of a broad IASCC crack. (B) BF-TEM of (111) orientated deformation twins extending from the crack tip. Corresponding DF-TEM of (C) parent austenite and (D) deformation twin.

Propagating IASCC cracks produce a deformation field that remains consistent for all cracks appertaining to each specimen tested at separate stress levels. These deformation fields in close vicinity to the cracks are added to the already existent heterogeneous plasticity field caused by the intense neutron-irradiation and the prior cold-work treatment to which the thimble tube was exposed to. Deformation caused by the irradiation was consistent with other microscopical investigations of highly irradiated materials [30, 31]. This irradiation-induced plasticity mostly resulted in dislocation entanglements and coarse dislocation

channels forming on the primary slip planes along the austenitic grains; the extent of which, ascertained further away from the cracks, did not differ significantly between O-rings tested to 60 or 80 dpa. Cold-working introduced a moderate degree of mechanical twins, uniformly distributed across the bulk, often interacting with nearby grain boundaries structures.

In close vicinity to the cracks, the deformation induced by the crack propagation at low stress levels in specimen TTO-1-053 (390 MPa) constituted of long-running parallel deformation slip and deformation twin bands adjacent to the cracks and corresponding crack tips [20]. Such deformation features were linked to the crack initiation and propagation of IASCC cracks, and extended from the crack flanks towards nearing grain boundaries. The density of twins was observed to increase closer towards the actual crack tip. On the other hand, relating to cracks extracted from specimens tested at high stress levels, similar but increased deformation features were observed within specimens TTO-1-001 (690 MPa) and TTO-1-090 (700 MPa - non-native oxide). In both cases, large sets of deformation twins were found to extend essentially in parallel from crack tip location into the bulk interior. The increased density of twinning at higher stress levels appear consistent with the grain boundary's ability to accommodate stress in the surrounding lattice. Fig. 2A shows an exemplary case for TTO-1-001 (690 MPa) of a high-stressed IASCC crack arrested at a grain boundary triple junction that displays a broad open crack morphology filled with intergranular oxides. Large sets of equivalent deformation twins with a twin face parallel to the (111) crystallographic planes can be observed adjacent to the crack. Under the influence of the stress exerted by the crack, the twin plane exemplifies a mirror section; the crystallographic indices of which can be calculated from [32] and are in agreement to the inset diffraction patterns displayed in Figs. 2C,D.

For TTO-1-090 (700 MPa - non-native oxide) displayed in Fig. 3A-B, another set of parallel twins propagating across the grain are shown, this time intersecting solely with the leading grain boundary. Adjacent to the grain boundary interface, a secondary twin system is also seen to nucleate, see Fig. 3C. Stress build-up at the grain interface may even cause a limited migration of the grain boundary itself, a phenomenon that seems consistent with diffusion-induced grain boundary migration (DIGM). The evolution of a grain boundary under the influence of stress, corrosion-enhanced diffusion or finite-volume displacive transformations, can cause it to locally propagate through one particular grain causing the simultaneous growth of the other adjacent grain [8, 33]. Effectively, this migration seems to be occurring only when two twin systems intersect simultaneously on either side of the interface with the grain boundary. Analysis of the set of twins customarily results in the typical twin-related diffraction pattern, see Fig. 3D. Both twin systems consist of a $< 111 >$ orientated twin plane as indicated by the demonstrated pattern indexation.

3.1.2. Crack tip investigations

Cracks extracted from the fracture and O-ring's outer surfaces generally resulted into a fully converged crack tips readily available for TEM investigation. Nu-

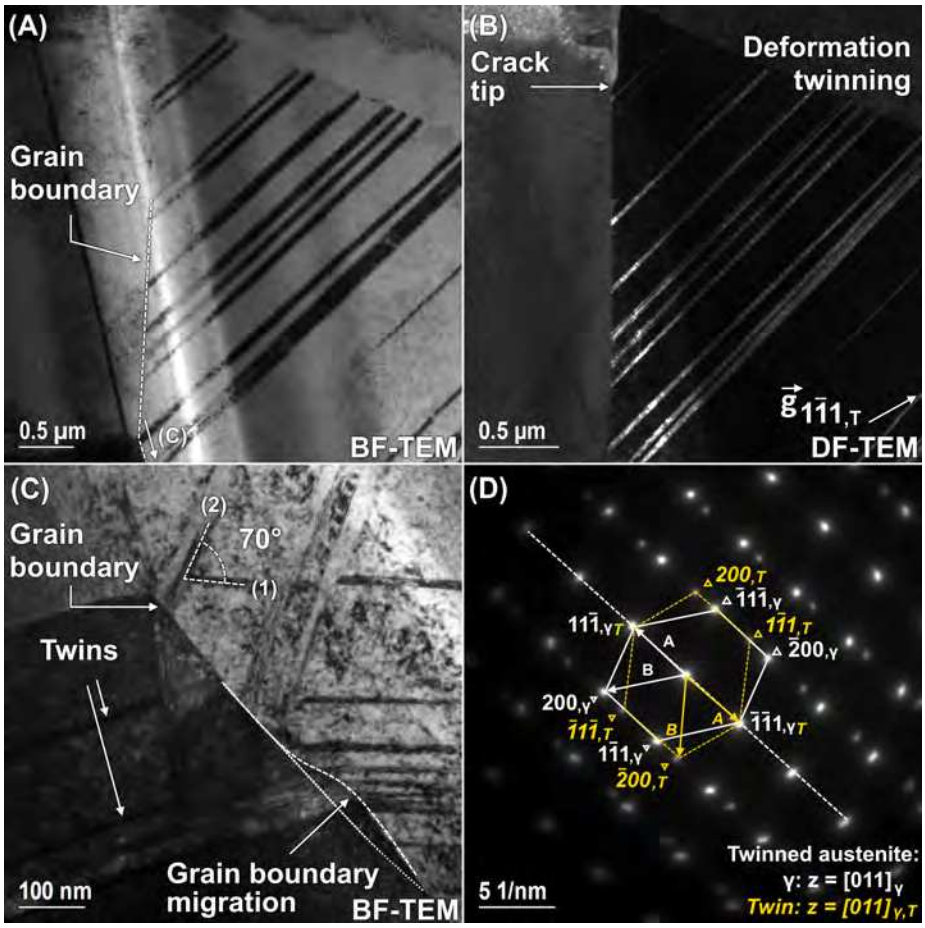

Figure 3: TTO-1-090 (700 MPa - non-native oxide) L01 (A) BF-TEM, and (B) DF-TEM of twinned microstructure ahead of an IASCC crack tip. (C) BF-TEM of double twin-systems leading to grain boundary migration. (D) Corresponding twin-related diffraction pattern.

merous crack tips were examined from all different specimens; several of which are shown from BF-TEM and inner oxidized DF-TEM perspective in Fig. 4. Recurring characteristics for crack tip morphologies include: (i) an asymmetrically oxidized crack front at low to intermediate stress levels as seen in Figs. 4A,B; facilitating the crack propagation in one of the adjacent grains more favorably than the other [20]. Cracking was observed to occur preferentially along the metal-oxide interface, presumably because the strained metal-oxygen bonds are inherently more chemically active and thus more prone to cracking. This observations at low stress levels appears consisted with prior literature observations [34]. On the other hand, cracks extracted from highly stressed specimens as seen in Figs. 4C-D, display more widened crack morphologies without showing any preferential cracking at the crack tip. Each crack illustrated (ii) thin oxidized

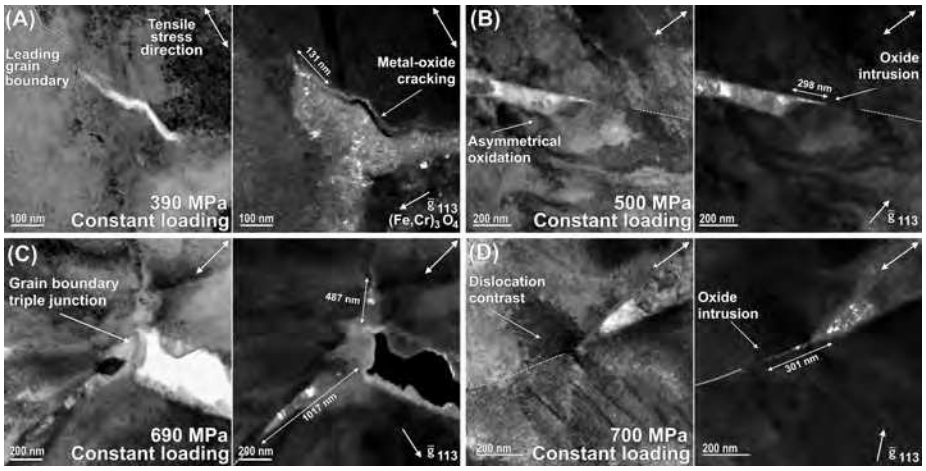

Figure 4: BF-TEM and corresponding DF-TEM of the oxidation in front of several crack tips corresponding to (A) TTO-1-053 (390 MPa) L03, (B) TTO-1-071 (500 MPa) L07, (C) TTO-1-001 (690 MPa) L16 and (D) TTO-1-090 (700 MPa - non-native oxide) L08.

crack flanks, often filled with a secondary corrosion product. Analysis of the oxide product is discussed in a subsequent paragraph and remained consisted with a chromite oxide analyzed in prior studies [20]. Our observations of thinly oxidized crack flanks are compatible with other microscopical examinations of IASCC cracks [35]. Furthermore, (iii) each crack converged into a fully oxidized crack tip with an oxidation length intruding into the leading grain boundary that seemingly increased with the applied stress. Indeed, as illustrated in Tab. 4, evident intrusion lengths at low levels of applied stress were measured to vary between a few hundreds of nanometers up to the order of about 1 μm in specimens subjected to higher stress. On par with the increased oxidation at one of the two neighboring grains, these oxide intrusions appeared to be correlated with strong deformation fields adjacent to the crack front near the grain boundary. It is reasonable that the lattice deformation and the local dislocation activity at the crack tip facilitated the intergranular oxidation, in addition to the known enhancing effects caused by the irradiated neutron-dose [36, 37] and applied levels of cold-work [38]. Observations of these oxide intrusions trigger a redefinition of what is implied by an intergranular crack tip; that is, it being referred to as the cracked oxide or the end of the oxide intrusion observed in the leading grain boundary.

A typical example of an oxidized crack tip is shown for specimen TTO-1-066 (280 MPa - cyclic loading) in Fig. 5A. The fatigue crack displays a fully oxidized crack tip wherein porous structures are observed, see Figs. 5C. Closer inspection from edge-on orientation using near-field Fresnel imaging shows that these porous structures consist of small oxidized fracture bands. It appears that these bands penetrate the oxidized region of the crack in such a manner that they may be associated with brittle cracking. Following the crack path, it is

Table 4: Overview of the intergranular chromite oxide intrusion depths measured for edge-on imaged crack tips appertaining to lamellae extracted from different stress-tested specimens (θ: angle between crack propagation direction and tensile stress direction).

Thimble Tube O-ring specimen	Mean (nm)	Maximum (nm)			Minimum (nm)		
Specimen ID	**Intrusion Length**	**Intrusion Length**	**Lamella ID**	θ	**Intrusion Length**	**Lamella ID**	θ
TTO-1-053 (390 MPa)	236	533	L01	14°	68	L08	2°
TTO-1-071 (500 MPa)	321	403	L11	2°	261	L03	74°
TTO-1-001 (690 MPa)	695	1259	L23	101°	305	L05	107°
TTO-1-090 (700 MPa - oxide removed)	222	301	L08	16°	120	L06	2°
TTO-1-066 (280 MPa - cyclic loading)	154	199	L09	20°	109	L07	16°

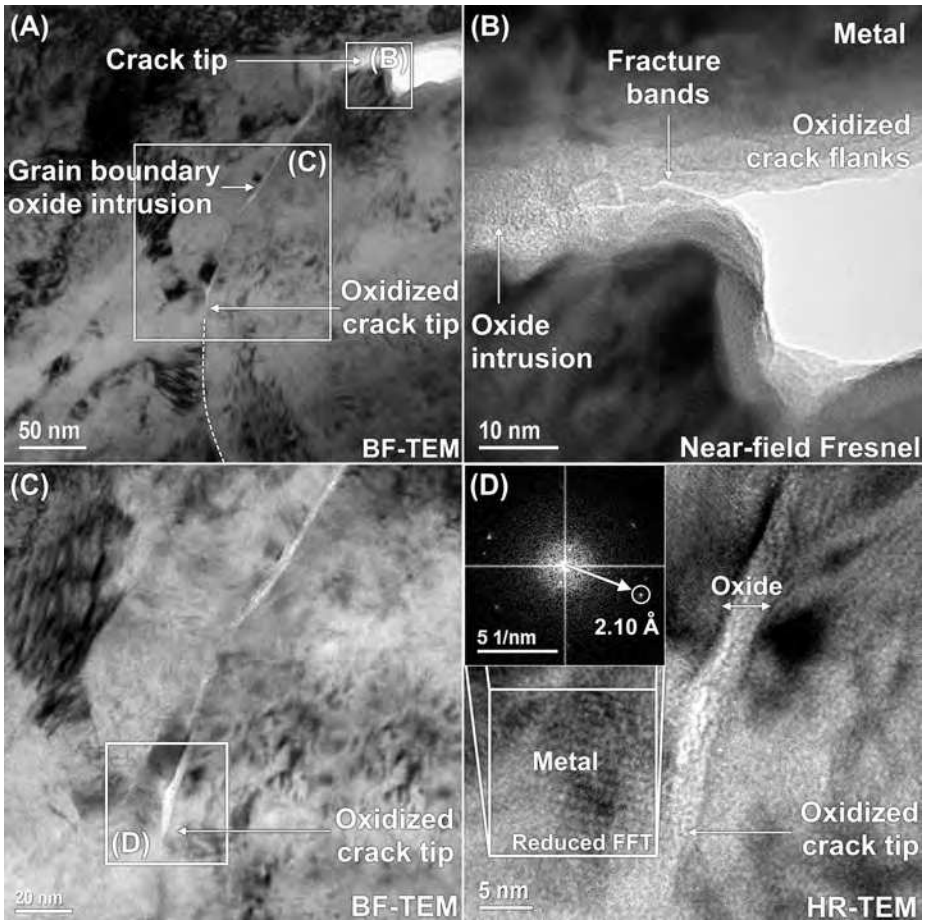

Figure 5: TTO-1-066 (280 MPa - cyclic loading) L09 (A) BF-TEM overview of grain boundary cracking whereat the oxide intrusion is seen to penetrate the leading grain boundary in front of the propagating crack tip. (B) BF-TEM underfocus Fresnel contrast image illustrating apparent fracture bands within the intergranular oxide. (C) BF-TEM of oxidized crack tip. (D) Corresponding HR-TEM of the crack tip. Inset FFT diffractogram illustrates the 111_{γ} austenite planes, while the oxidized tip remained amorphous.

evident how the internal oxide closely intrudes in the grain boundary interface. The oxide intrusion extends for over 200 nm in length and broadens for only several nm's in width. This needle-like intrusion results into a final oxidized crack tip as shown in Fig. 5C. Due to the narrow width of oxide intrusion, it remained difficult to fully isolate diffraction reflections from the internal oxide from those of the neighboring bulk metal in a single objective aperture during SAED imaging. Additional investigation using HR-TEM imaging reveals the metallic crystal lattice at atomic resolution while the oxidized crack tip remained fully amorphous, see Fig. 5D.

3.2. Cyclic loading

3.2.1. Twinned microstructure

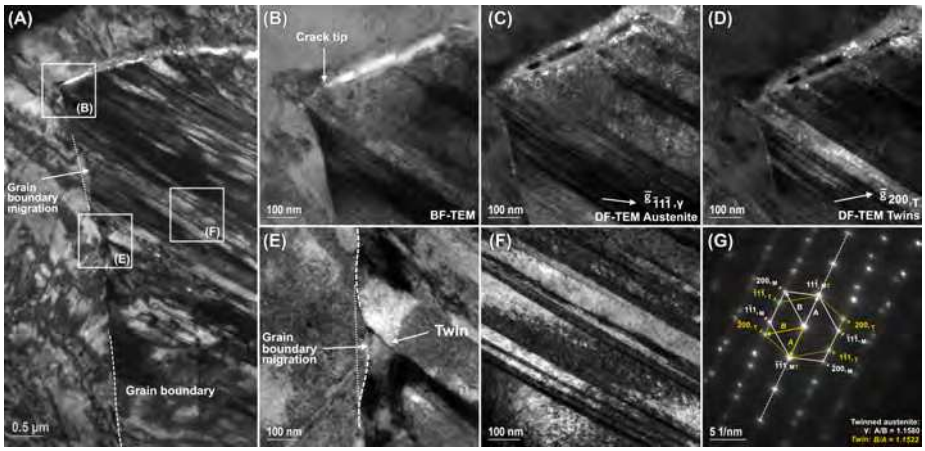

Figure 6: TTO-1-066 (280 MPa - cyclic loading) L09 (A) BF-TEM overview of twinned microstructure in the crack's near vicinity. (B) BF-TEM and (C,D) DF-TEM of the austenitic and twinned microstructure, respectively. (E) Grain boundary migration. (F) BF-TEM of twins and (G) its corresponding diffraction pattern.

Examination of the microstructure in close vicinity of fatigue cracks appertaining to the cyclic loaded sample indicated a severely twinned deformation field with evidence of shear and stress-induced martensite bands. Fig. 6A illustrates a global overview of the impact of twinning on the crack and its leading grain boundary interface. Regions of strain contrast indicating stacked dislocation pile-up at sheared regions in between deformation twins are evident adjacent to the crack. Figs. 6B-D illustrate the extent of the twinning on the cracked grain boundary interface. Deformation twins may also have a displacive impact on the austenitic microstructure which can result in the curvature of a propagating crack, or the effective migration of its leading grain boundary, as observed in Fig. 6E. Grain boundary migration is again observed in association with a secondary twin system nucleated in the opposing grain. To that end, the microstructural evolution surrounding fatigue cracks is similar, although substantially more intensified, as observed in highly stressed specimens. SAED imaging of the microstructure revealed the typical twin-related diffraction pattern, see Fig. 6G.

3.2.2. Martensitic transformation

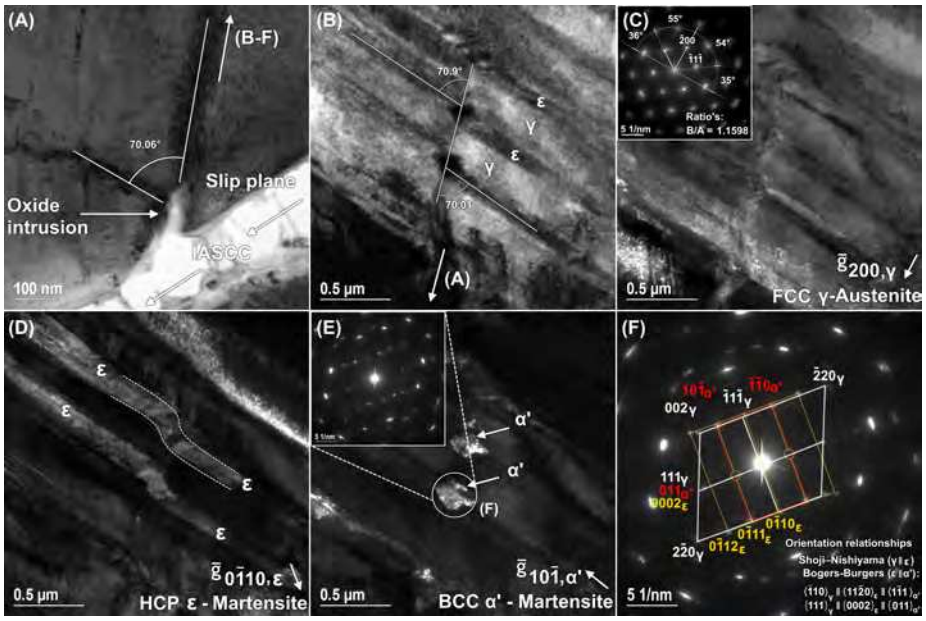

Figure 7: TTO-1-066 (280 MPa - cyclic loading) L08 (A) BF-TEM of ϵ-martensite laths extending from the crack flanks into the bulk interior. Deeper into the bulk, phase transformation of austenite to martensite is observed in accordance to Olsen-Cohen's model [39] from a (B) BF-TEM, and (C-E) DF-TEM γ-austenite, ϵ-martensite and α'-martensite perspective. The overall diffraction pattern is illustrated and indexed in (F).

Notable deformation structures that resemble phase-transformed austenite to martensite can be observed within the microstructure in close vicinity to propagating cracks. Fig. 7 shows two characteristic hcp ϵ-martensite deformation laths extending from a fatigue crack flank, for which one forms adjacent to a deformation slip band extending into the bulk. The angle between both ϵ-laths is equivalent to the angle of the close-packed high-symmetry crystallographic 111-planes of the parent austenite (i.e. around 70°) on which ϵ-martensite laths are known to preferentially nucleate [40]. Interestingly, attributed to the high dislocation density within the adjacent deformation slip band, a preferential intrusion of intergranular oxides can be observed into the bulk matrix. Further into the bulk, other instances of austenite to martensite phase transformations may be observed adjacent to microstructural slip bands, see Figs. 7B-D. The ϵ-martensite laths make the typical wavy shear interaction described in the Olsen-Cohen model for martensitic transformations [39]. At this shear interaction, Figs. 7E shows the stress-induced nucleation of bcc α'-martensitic islands in the parent austenite. DF-TEM images in the current showcase were made by means of diffraction spots belonging to the different phases, from which Fig. 7F reveals the schematic representation of the Shoji-Nishiyama $\gamma \parallel \epsilon$ (S-N) and Bogers-Burgers $\epsilon \parallel \alpha'$ orientation relationships:

$$\{111\}_\gamma \parallel \{0002\}_\epsilon, (Shoji - Nishiyama, Fig.7F)$$
$$< \bar{1}10 >_\gamma \parallel < 11\bar{2}0 >_\epsilon$$
$$\{0002\}_\epsilon \parallel \{011\}_{\alpha'}, (Bogers - Burgers, Fig.7F)$$
$$< 11\bar{2}0 >_\epsilon \parallel < 1\bar{1}1 >_{\alpha'}$$

3.3. Non-native oxide crack characterization

3.3.1. Crack morphology

BF-TEM investigation of IASCC cracks belonging to the non-native oxide specimen generally displayed a crack morphology that gradually tapers down from a uniformly oxidized triple junction or fracture surface. Crack flanks at the metal interface are consistently oxidized by a thin primary nanocrystallite oxide film, while a coarse-grained secondary oxide is typically observed in more wide open crack regions. Void spaces may be observed in between the duplex oxide assembly near the fracture surface where crack opening is consistently wider. The tapering of the crack may continue for several tens of μm's, leading to a fully developed intergranularly oxidized crack tip. Cracks may establish branch points at microstructural grain boundaries along the way, typically in a cleavage relation to the applied tensile stress direction. Intergranular oxidation at these branch points recurs at every interaction. As the crack narrows, less of the corrosion product and more of the nanograined oxide is observed until only a uniformly oxidized crack tip remains.

3.3.2. Oxide analyzes

Figs. 8A,B display an overview of a typical IASCC shear crack propagating from a uniformly oxidized fracture surface, extending up to a bulk grain boundary triple junction. Major characteristics are the long and tapered crack appearance and its duplex oxide formation within the crack opening. The crack itself is comprised of a nanograined oxide with a thickness close to 100 nm on both opposing sides filled by a coarse-grained oxide deposit, see Fig. 8C. EDS spot- and SAED diffraction analyses respectively shown in Figs. 8D and 8E-F demonstrate that the crack flank oxide corresponds to a Fe- and Cr-rich spinel with a ring-like diffraction pattern signifying its nanograined crystallite structure, while Figs. 8G-H show that the deposited oxide solely exhibits an Fe-rich spinel with a disparate spot-like diffraction pattern. Both diffraction patterns correspond to a face-centered cubic (fcc) crystal structure with similar lattice constants experimentally valued to be 0.8372 nm and 0.8396 nm, respectively. To that end, it may be concluded that the non-native duplex oxide is composed of the $(Fe,Cr)_3O_4$ chromite [41] and the $(Fe,Ni)_3O_4$ magnetite [42], and that it is structurally no different from the oxides previously investigated in other O-ring specimens [20]. Additionally, in further agreement with this study [20], is that the crack preferentially corroded a MnS particle segregating close to the grain

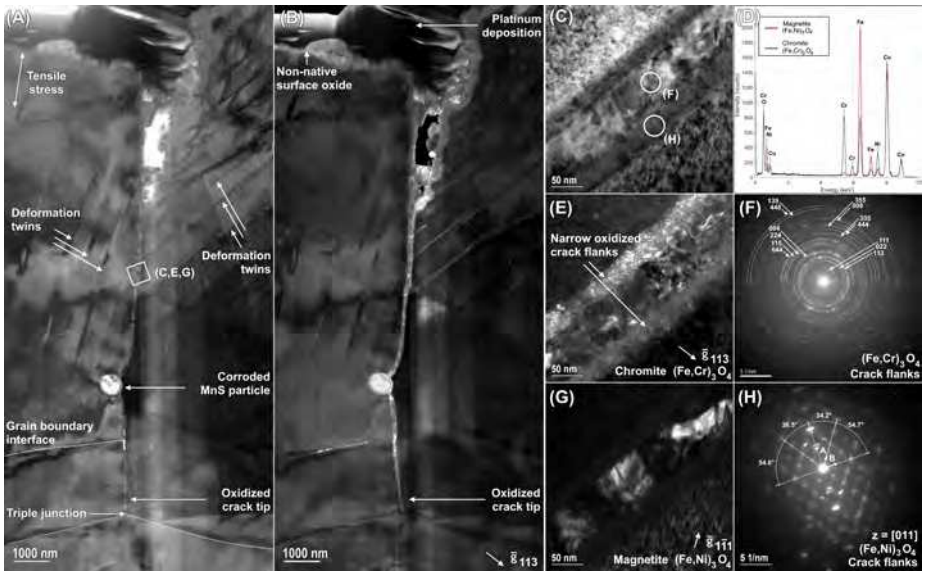

Figure 8: TTO-1-090 (700 MPa - non-native oxide) L06 (A) BF-TEM and (B) corresponding DF-TEM of the general crack morphology imaged from an internal chromite reflection. (C) BF-TEM of narrow oxidized crack flanks. (D) EDS spectra of the duplex oxide formation inside the crack flank of C. (E-F) Chromite $(Fe,Cr)_3O_4$ and (G-H) Magnetite $(Fe,Ni)_3O_4$ DF-TEM and corresponding diffraction patterns relating to C.

boundary. Although, contrastingly to the previous case, the crack demonstrated in Fig. 8 ultimately did not come to a full arrest at the particle. It is therefore expected that a MnS particle only impedes upon the crack propagation, but due to prolonged exposure, cracking is allowed to continue until some other type of arrest occurs. Consistent with most cracks observed within this study, this arrest occurred at a grain boundary triple junction orientated near perpendicularly upon the crack propagation direction.

3.3.3. STEM-HAADF investigations

Fig. 9 demonstrates the most relevant STEM-EDS chemical maps of the IASCC crack tip and its leading grain boundary interface depicted in Fig. 3. Clear depletion of Fe and Cr may be observed in front of the crack tip, while evident enrichment of Ni is apparent at the crack tip location. Ni is observed to enrich adjacent to the crack flanks and further along at a distance of several tens of nm's in front of the crack tip. Additionally, elemental spectra of Mn and Mo show an evident depletion in front of the crack tip in agreement with previous observations [43]. Furthermore, small Ni and Si clusters were also observed throughout the matrix in equal densities close and far away from the crack tip. This observation signifies that their presence is unrelated to any of the deformation mechanisms relating to the crack propagation. Rather, their origin can be related to the small coherent diffusion of structural elements following the intense effects of neutron-irradiation. Indeed, rough estimated diffusion distances of RIS tend

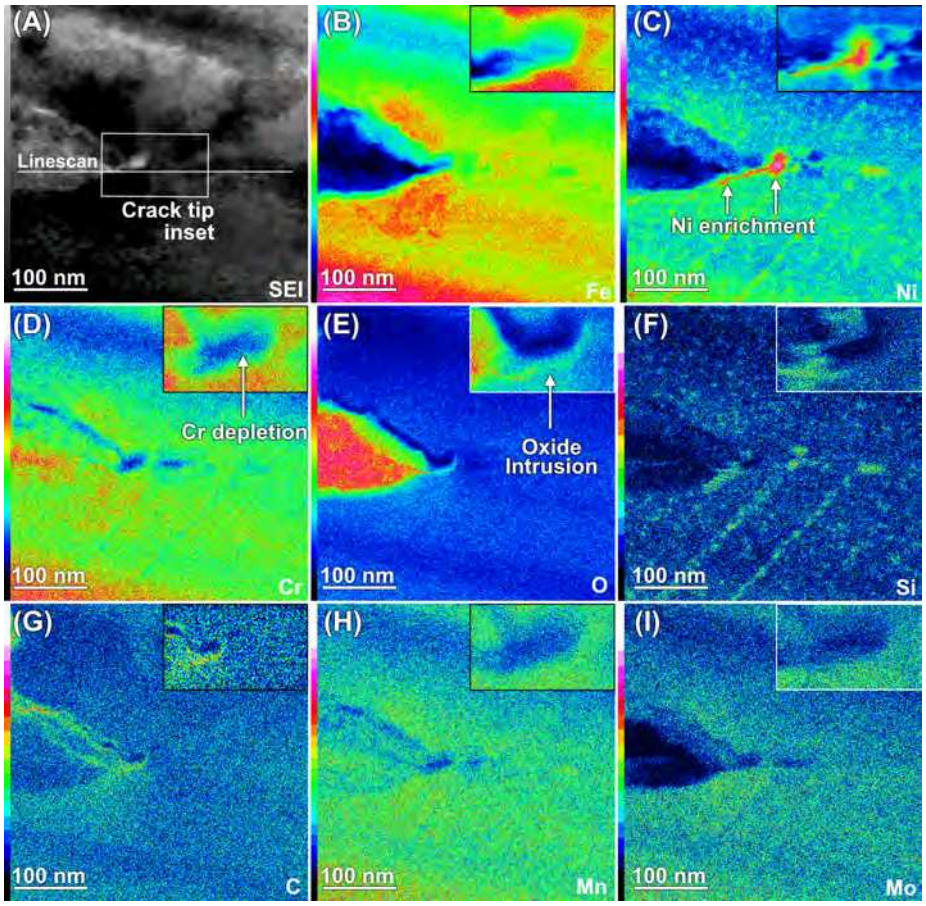

Figure 9: TTO-1-090 (700 MPa - non-native oxide) L01 HAADF-STEM EDS chemical mapping of enriched and depleted elements close to a selected IASCC crack tip. Regions of high to low STEM intensities are indicated by the color scheme varying from white to black, respectively.

to show that elemental diffusion lengths are of the order of around several to tens of nm's [44, 20], which reasonably corresponds to the clusters' approximate size distributions. Moreover, the deformation field is also seen to cause some inhomogeneous segregation and depletion of structural elements at the grain boundary interface. Indeed, Ni but also more evidently Si, are observed to effectively enrich at separate locations along the grain boundary corresponding to the local impact of intersecting twin systems. Chemical enrichment of these elements is also evident at the twin interfaces themselves. Pertaining solely to oxide concentration map, it is evident how the crack tip itself is completely filled by the chromite oxide. It is unmistakable how oxide intrusions extend into the leading grain boundary in the form of a nm-wide needle-like oxide intrusion, similar to what has been observed in Fig. 5. Since oxidation in front of the

crack tip was evident from all crack tips observed in Fig. 4, this additional result signifies that oxidation embrittlement may contribute significantly towards the genuine propagation of the IASCC crack.

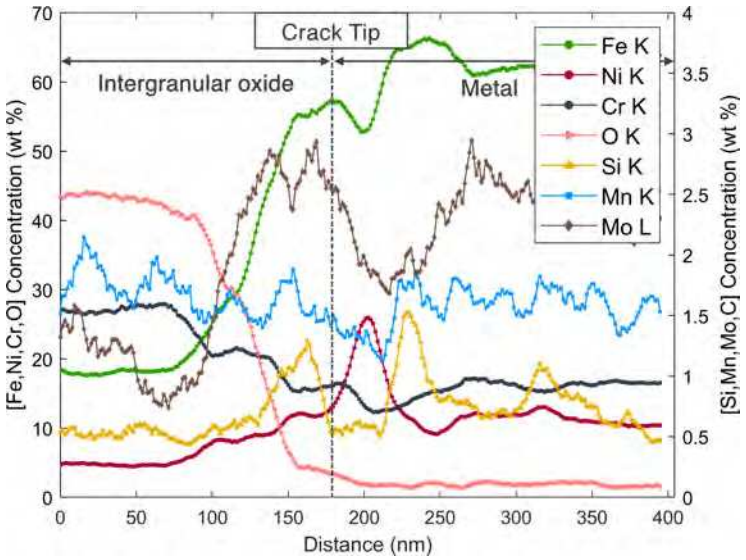

Figure 10: TTO-1-090 (700 MPa - non-native oxide) L01 HAADF-STEM EDS line scan along the IASCC crack tip propagation direction illustrated in Fig. 9A.

Fig. 10 reports the chemical concentrations following the crack tip propagation direction of the crack displayed in Fig. 9. It is evident from the structural element profiles that Fe and Cr transition from their oxidized form prior to the crack tip to their bulk concentration values, in a rather inconsistent manner. This suggests that there is a complex chemical interaction between other contributing elements at the crack tip. Indeed, first and foremost, clear depletion of Fe and Cr may be observed at the crack tip location, while Ni enriches to values of near 26 wt. % (+103% vs. metallic concentration). Secondly, it is observed that the crack tip oxide concentration drops at a steeper rate compared to the corresponding Cr concentration, and that lower values of Cr are detected close to the crack tip location. This may indicate the crack tip's ability to form a poorer Cr-oxide susceptible to brittle fracture. Furthermore, it is apparent that local deformation close to the grain boundary greatly influences the chemical composition of the grain boundary itself. For instance, Si is enriched at three separate locations in the oxidized part (+144% vs. oxidized concentration) and at the metallic part (+189% and +109% vs. metallic concentration) of the crack, each corresponding to the local impact of twins intersecting with the grain boundary interface. As seen in Fig. 9F, Si may enrich just as equally at twinned interfaces, as they may act as microstructural sinks for RIS. Similarly for Mn and Mo, their concentrations show some depletion behind the crack tip consistent to what has been observed in prior analyzes [20].

4. Discussion

4.1. On the effect of applied external stress

Influence of the active stress state on the initiation and propagation of IASCC cracks may first be derived from the crack overview table listed in Tab. 3. Primarily, it is evident that crack propagation was facilitated by the applied tensile stress while it acted upon the crack in cleavage-mode orientation. Contrastingly, crack tips propagating in the otherwise shearing-mode orientation were found to be arrested far more frequently. These observations are reminiscent of previous studies where an influence of the tensile stress was also found to play a role [20, 45]. Likewise, in consideration of the acting stress value, it was evident that crack branching at oxidized triple junctions occurred more frequently in lower stressed specimens compared to otherwise higher stressed specimens. Moreover, as was observed from TTO-1-053 (390 MPa) [20], branching occurred more frequently at triple junctions where one grain boundary was orientated favorably with respect of the tensile stress. It is possible that crack branching at lower stresses occurs more easily within specimens exposed longer to the corroding environment where the crack is given more time to develop.

From microstructural examinations, it was further observed that deformation twins extend from the crack flanks into the bulk matrix. Especially at higher stresses, larger densities of deformation twins were empirically observed in close vicinity of the crack tip, see Fig. 2. Observations of twinning well-below the irradiated yield stress ($\approx$ 1000 MPa) suggests that the nucleation of deformation twins occurs as a consequence of the lattice deformation induced by the propagation of the crack [20]. Apart from the twinning at the crack tip, multiple twin systems were also seen to interact with the leading grain boundaries further away from the tip, see Fig. 3. These transformations are often accompanied with the abrupt migrations of the grain boundary interface, which is induced by the deposition or removal of solutes from the matrix [46]. This phenomenon is otherwise described as diffusion-induced grain boundary migration (DIGM) [46, 47]. The growth of one crystal grain at the expense of the other in association to DIGM, has been observed in previous investigations involving crack growth under the influences of external stresses [8, 33]. DIGM may hint towards the contribution of IASCC-relevant phenomena such as grain boundary sliding [48] and separation [30]. Indeed, stress build-up in a mobile segment of the grain boundary enhanced by the diffusion of solutes contributes to this migration. To that end, DIGM may promote several dissociation reactions of the grain boundary interface, ultimately leading the way for possible intergranular crack initiation.

DIGM should also be contemplated with respect to the chemical composition of the grain boundary interface, especially in relationship with the intersecting twinning systems that were observed ahead of the crack tip in Fig. 3. These twins were found to be enriched by Ni and Si while also inhomogeneously affecting the local grain boundary chemistry ahead of the crack, see Fig. 9. If the enrichment of twin interfaces is due to the processes of RIS, then this signifies that they

already nucleated prior to the initiation of the crack and therefore do not stem from the crack propagation itself. In this respect, it is important to note that local stress caused by the lattice deformation of the expanding deformation twin can concentrate at the grain boundary interface. In association with DIGM, this stress build-up may further enhance the susceptibility to intergranular cracking [45, 49]. In agreement with the study on twinning systems in fcc metals, Rémy [50] indicated that readily present twins interacting with the grain boundary may lead to crack initiation sites as well as facilitate the propagation of already nucleated cracks. An additional factor to consider is that deformation twins may forcefully lead to potential transgranular propagation of cracks, although this was not observed.

4.2. Stress-assisted oxidation at the crack tip

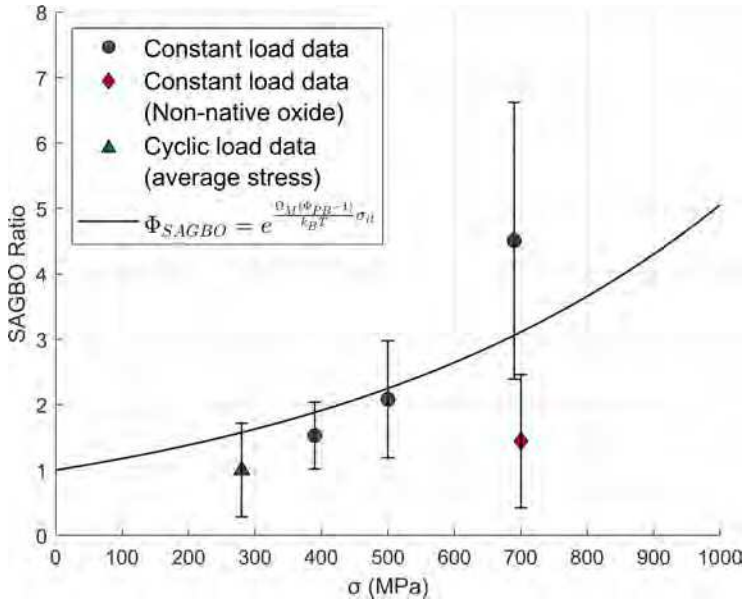

Figure 11: Mean intergranular oxidation lengths with corresponding standard errors on the oxide intrusions measurements, normalized to the specimen with the lowest macroscopic stress, for crack tips extracted from O-rings tested under increased stress conditions.

Intergranular oxidation ahead of propagating crack tips in stainless steels subjected to PWR conditions has been observed on several occasions [20, 34, 51, 52]. Although it was readily predicted that the effective stress concentration at the crack tip facilitated the crack tip oxidation [34, 53], to the best of our knowledge, no such stress-dependent effect has yet been empirically revealed. To that end, Figs. 4 and 5 demonstrate prime examples of IASCC crack tips showcasing oxide intrusions into the leading grain boundary; the lengths of which, for crack tips appertaining to specimens tested under increasing stress conditions, are displayed in Tab. 4. At low levels of applied macroscopic stress, oxidation in

front of the crack tips remains moderately comparable to known literature data [43]. Under these conditions, the oxidation is mainly determined by the effects of the high neutron-irradiation doses [37, 36] and prior cold-work treatment [38], both having shown to increase the oxidation rates in laboratory experiments. However, as the applied macroscopic stress increases, an effective increase in mean oxidation length in front of the crack tips can be observed. In Fig. 11, the average oxide intrusion lengths in front of the crack tip is displayed, normalized to the average value of the sample with the lowest stress as a function of stress. The normalization of the data is performed in order to solely illustrate the increase as a consequence of increasing tensile stress. This trend demonstrates an exponential effect; a phenomenon which is reminiscent of Evans's stress-assisted grain boundary oxidation model (SAGBO) [54]. Accordingly, the acting stress at the crack tip may assist in the transport of diffusive corroding species within the intergranular oxide along diffusion paths constituted of internal oxide defects. Empirical observations of thin fracture bands within the intergranular oxide at the crack tip, as seen in Fig. 5B and our previous work [20], may be deemed as such fast-diffusion paths for the intergranular oxide species [51]. To assess the stress-assisted oxidation along the crack tip, the SAGBO model evaluates the growth rate of the oxide intrusion in the stressed state $\dot{\ell}_\sigma$ with respect to its growth under a stress-free condition $\dot{\ell}_0$, as Φ_{SAGBO}:

$$\dot{\ell}_\sigma \propto \frac{D_v C_{it}}{\ell} \exp\left[\frac{\sigma_{it}\Omega_M(\Phi_{PB}-1)}{k_b T}\right] \tag{1}$$

$$\Phi_{SAGBO} = \left(\frac{\dot{\ell}_\sigma}{\dot{\ell}_0}\right) = \exp\left[\frac{\sigma_{it}\Omega_M(\Phi_{PB}-1)}{k_b T}\right] \tag{2}$$

whereat σ_{it} represents the tensile stress at the oxide intrusion tip in front of the crack tip, Ω_M the total metal alloy volume (calculated from 316SS's molar volume [55] as $1.16e-29$ m^{-3}), Φ_{PB} the Pilling-Bedworth ratio (known to be around 2.07 for chromium oxides at the crack tip [56]), k_B Boltzmann's constant, and $T = 593$ K the ambient PWR testing temperature.

Extrapolating the stress-assisted oxidation effect from a state of zero-effective stress in accordance to equation 2 is displayed in Fig. 11. In first approximation, the stress intensities at the oxide intrusion tips σ_{it} are evaluated equal to the O-ring's macroscopic tensile stresses along the fracture surface. However, stress concentration at the crack tip, as a consequence of the deformation-induced twinning plasticity, local dislocation activity, or surrounding grain orientation, may lead to an even more increased effect as is currently predicted. Still, by taking the standard material input parameters, the stress-assisted enhancement factor correlates well with the increase in the normalized average intrusion lengths displayed in Tab. 4. The oxide intrusion lengths markedly increase by a factor of 5 with a local stress of 1000 MPa predicted at the oxide inclusion tip. However, the distinct outlier corresponding to the intrusion lengths of TTO-1-090 (700 MPa - non-native oxide) does not stroke with the trend curve and is

possibly related to an overestimated stress at the crack tip (see the discussion in the subsequent paragraph).

Our observations could be differentiated from the limited available literature data on crack tip oxidation in stainless steels [35, 57, 58, 43]. Typically reported oxide penetration depths ahead of propagating tips are of the order of hundreds of nm's, whereas in this study a record value of over 1 μm is reported within the highest stressed specimen. This variation could be reasoned in terms of varying material and testing conditions, exposure times to the corrosive environment, and due to the effective stress concentration at the crack tip. It is further assumed that the high irradiated doses of the flux thimble tube material ($60-80$ dpa) and its applied level of cold-work (20% CW) have significant impacts on the oxidation rates at the IASCC crack tip [37, 36, 38]. Observations of these crack tips have also indicated towards microstructural features that are considered as evidence of fast-diffusion paths for oxygen species [51]. Most significantly, these features relate to the high densities of defect clusters signified by the increased dislocation contrast around the crack tips and the evidence of brittle fracture bands within the oxide intrusions. When every observation is taken into account, our findings clearly demonstrate that under the SCP regime the intergranular oxide grows faster than the crack propagation rate. Moreover, our results provide strong support for a stress-driven internal oxidation mechanism that describes the oxide embrittlement of the leading metallic matrix ahead of an advancing crack [8, 17, 18, 19, 59]. Intergranular oxides are then reasoned to be responsible for the lowering of the fracture resistance at the grain boundary, providing a facilitated means for intergranular crack propagation within the leading oxide intrusion.

4.3. Mechanical failure data

The following discusses how the previous findings contribute to the failures of O-rings with an abrased outer oxide surface and those being subjected to cyclic loading. Fig. 12A displays their failure times as a function of stress in correlation with the other constant-load stress tested O-rings. The corresponding trend curves drawn for each dataset are represented by dashed lines, calculated in accordance to the proportionality ratio between TTFs and failure stress, given by equation 4. This ratio is developed in relation to the subcritical crack propagation model by Konstantinović [16], and is dependent on the cracking susceptibility parameter n. Fundamentally, this parameter stems from the empirical power law for crack growth and essentially denotes a material's susceptibility to cracking [61]. Within the SCP model, the higher the value of n, the more reliable a material's resistance to fracture. To that end, the cracking susceptibility parameter is a good measure for correlating the TTFs for specimens tested to different sample conditions. Respectively, each curve is drawn for the statistically optimized cracking susceptibility parameter n, correlating the TTFs at any point with the respective failure stress.

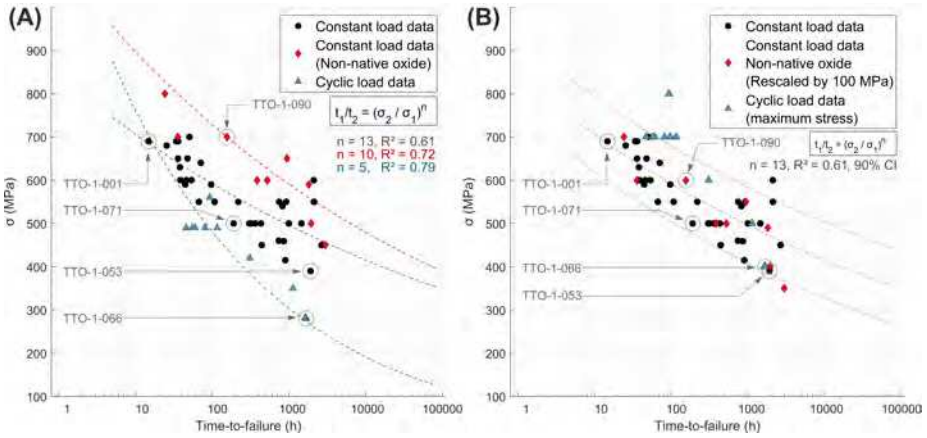

Figure 12: (A) Overview of the TTFs of the constant load native, non-native, and cyclic loaded O-ring data in terms of stress [60]. Regression analysis of data is performed through equation 4, statistically optimized to match the most ideal SCC corrosion susceptibility parameter n. (B) Adjusted stress interpretation of the non-native oxide and cyclic loaded O-ring failures on the account of possible crack initiation from the O-ring's inner surface and peak stress intensity values, respectively.

$$t \propto \frac{1}{\sigma^n} \tag{3}$$

$$\frac{t_1}{t_2} = \left(\frac{\sigma_2}{\sigma_1}\right)^n \tag{4}$$

4.3.1. On the effect of oxide abrasion

As observed in Fig. 12A, the apparent shift rightwards to higher TTFs reveals that the non-native oxide specimens are less susceptibility to IASCC failure after the removal of the native PWR oxide layer on the outer O-ring's surface. Non-native oxide specimens are seen to fail at a later point in time under a given stress state, or equally, at higher stresses under a preset TTF compared to other native oxide specimens. The best-fit cracking susceptibility parameter for non-native oxide specimens lowers to $n = 10$ in comparison to other constant load compression tested O-rings with their native oxide intact. This change indicates that the removal of the outer surface oxide has altered some aspect of the cracking mechanism in relation to the other constant-load specimens.

From the microstructural investigation, Fig. 8 revealed that the duplex oxide formed along the crack flanks of TTO-1-090 (700 MPa - non-native oxide) constitutes of the same oxide morphology as observed in other specimens [20]. However, as illustrated in Fig. 11, cracks from TTO-1-090 (700 MPa - non-native oxide) produced comparatively less oxidized intrusion lengths in front of the crack tips as should be expected in accordance to the SAGBO model [56]. Intergranular oxidation in the non-native oxide specimen therefore does not stroke with the

expected oxidation lengths at the given stress state in comparison to other specimens. Accordingly, this difference could be related to a lower stress-enhanced oxidation at the crack tip; possibly in relation to the initiation of cracking in regions of the O-ring where lower effective stresses occurred. Indeed, finite-element modelling of the Von Mises stresses have shown that the inner part of the O-ring constituted to a lower effective maximum stress during the compression testing than the outer surface [15]. Arguably, following the abrasion of the outer surface oxide, crack initiation may have occurred from the lower stressed inner surface as opposed from the anticipated outer surface instead. The probability of crack initiation from the inner surface whereat a sufficiently saturated oxide formed under aerated conditions still remained, may have increased during testing. This observation is explicated from the view of the SCP process wherein crack initiation in brittle oxides is dominated by the inherent structural flaws that exist within these oxides. The probability of cracking tends to be effectively greater in more voluminous oxides. Consequently, following the initiation from the inner surface, the lowered oxide intrusion lengths are thus interpreted by the reduced stresses that take place near the crack tips at the point of initiation. In this reasoning, it can be argued that the O-ring failures with the non-native oxide surface must be plotted against an overestimated critical stress in the mechanical failure data displayed in Fig. 12B. Indeed, by lowering the stresses by an arbitrary value of about 100 MPa, all TTFs of the non-native oxide specimens shift into the confidence interval of the other constant-load O-ring specimens.

Consistent with the observation of crack initiation from the O-ring's inner surface following the abrasion of the outer surface oxide, is that the onset of cracking at all times could not be ruled out in either failed or non-failed O-ring specimens [20, 60]. This observation is in agreement with evidence from the available literature, which shows that crack initiation within O-ring specimens was seen either from the anticipated outer surface, from the less anticipated inner surface, or within both [62].

4.3.2. On the effect of cyclic loading

Concerning the TTFs of cyclic loaded O-rings, it was observed by Bosch et al. that the stress threshold below which no IASCC failure occurs under constant loading, shifts from about 40% [15] down to only 19% of the irradiated yield stress under transient cyclic loading [28]. In that regard, cyclic loading was argued to have a detrimental effect on the component lifetime and thus on the IASCC susceptibility of tested O-rings. Similar conclusions can be drawn from the TTFs and the corresponding trend curves for constant and cyclic loaded O-rings displayed in Fig. 12A. Evidently, the cyclic failures occur at a significantly lower stress as compared to constant loaded specimens. This decrease is encapsulated by a much steeper trend curve in the regression analysis of the failure trend curves. Expressed in terms of the SCC susceptibility parameter n, a drastic change from constant ($n = 13$) to cyclic loading conditions ($n = 5$) can be observed. This transition suggests that material fatigue may influence the cracking in ways under cyclic loading that were not the observed under common constant load

conditions. However, one has to take into account the fact that the TTF of the samples tested under cyclic loading are represented by an average stress. Since the crack tip oxidation results discussed in the previous sections indicate that stress plays the most significant role for oxide formation, one can safely assume that maximum stress during each transient load cycle needs to be taken into account as a proper parameter to interpret the failures under cyclic loading. Indeed, by plotting TTF data under cyclic loading against maximum stress, all data shift upwards in stress into the predicted failure regime delineated by the confidence intervals of constant loaded specimens, see Fig. 12B. To that end, it may be argued that crack propagation is facilitated at the peak stresses, which may then lead to shorter TTF during cyclic loading.

From the microstructural analysis, the change in cracking mechanism under cyclic loading becomes evident from the analysis of IASCC cracks stemming from specimen TTO-1-066 (280 MPa - cyclic loading). Indeed, cyclic crack propagation has been linked to hydrogen-assisted fatigue cracking [13], especially in relation to the formation of susceptible martensite phases adjacent to crack flanks. Microstructural analyses have shown stress-induced austenite to martensite phase transformations adjacent to fatigue cracks in accordance to the Olsen-Cohen model, see Fig. 7. Martensite phases are typically promoted under high stressed conditions [63, 64, 65, 66] in association to presence of hydrogen [13, 67]. Especially following the exposure to a PWR environment, mobile hydrogen may diffuse into the crack and segregate at leading crack tip grain boundaries. Its presence promotes and increases the formation of hcp ϵ-martensite laths while under the influence of straining [13]. In accordance to Bogers formalism [68], aggregated bcc α'-martensite islands may then nucleate following the shear interactions of two ϵ-martensite bands within the parent austenitic phase. Prior observations of martensite phases at the crack tips of fatigue cracks in SS304L are in support of this reasoning [13] and fully correspond to the findings displayed in Fig. 7. On the presence of martensites with regards to the cracking aspects, it is known that strain-induced α'-martensite not only has a higher strength [69] but also a larger volume per atom [70] than the parent austenite matrix. This may create a considerable amount of internal coherency strains, which increases the susceptibility to fatigue cracking overall [13]. In agreement with the mechanical load testing, the martensitic phase transformation following cycling fatigue leads to a decreased fatigued life-time.

Further microscopical investigations have also shown a substantially more deformed microstructure near the crack tip and along its leading grain boundary. Fig. 6 shows the neighboring grain's ability to bear large amounts of shear by developing deformation-induced twins in close vicinity to the intergranular crack. At sufficiently high stresses, these deformation products are known to form along finite-volumes of the close-packed 111 high symmetry austenitic planes. The displaced lattice volumes that they induce, can effectively impede on the dislocation glide path and thus contribute to the transformation strengthening of the material [24, 25]. When the critical twinning stress is reached, dislocations may pile up at deformation-induced twin interfaces, leading to consequent strain

hardening [69] and an increased susceptibility to brittle fracturing. This process is expected to be enhanced by the peak stress intensities at the crack tip occurring during each consequent load cycle. Reasonable estimates of the SAGBO parameter at these maximum stress intensities still show a good agreement with the expected oxidation lengths in Fig. 11.

5. Conclusions

In the evaluation of the crack tip and microstructural properties of cracks appertaining to O-rings tested under (i) increasing stress, (ii) native against non-native surface oxide, and (iii) constant load against cyclic fatigue load conditions, the following conclusions may be reiterated:

(i) Crack tip advancement is seemingly driven by thin oxide fracture bands and nanometer wide oxide intrusions into the leading grain boundary interface. All observations support the subcritical crack propagation [16] models.

(ii) Oxidation lengths in front of active crack tips are evidently increased by the presence of external tensile stress. The increase corresponds to the phenomenon best described by stress-assisted grain boundary oxidation [54].

(iii) Intergranular cracks appertaining from non-native oxide O-ring specimens illustrate comparatively less oxidized crack tips in relation to other high stressed specimens, which could indicate towards initiation of cracking from the O-ring inner surface where lower effective stresses occur. This observation fittingly agrees with the overall shift to higher TTFs observed from the macroscopic load TTF data of other non-native oxide specimens.

(iv) Cyclic loading is observed to promote the IASCC cracking as evidenced by the lower TTFs in the macroscopic failure data, and the increased twin-deformation and martensitic transformation features at and around the crack tip.

Acknowledgements

This work is supported by ENGIE Electrabel under grant agreement No. BENGIE5500.

References

[1] P. Scott. 2000 F.N. speller award lecture: Stress corrosion cracking in pressurized water reactors interpretation, modeling, and remedies. *Corrosion*, 56, 08 2000.

[2] P. L. Andresen. Emerging Issues and Fundamental Processes in Environmental Cracking in Hot Water. *Corrosion*, 64(5):439–464, 05 2008.

[3] G. S. Was and P. L. Andresen. Stress Corrosion Cracking Behavior of Alloys in Aggressive Nuclear Reactor Core Environments. *Corrosion*, 63(1):19–45, 01 2007.

[4] S.M. Bruemmer, E.P. Simonen, P.M. Scott, P.L. Andresen, G.S. Was, and J.L. Nelson. Radiation-induced material changes and susceptibility to intergranular failure of light-water-reactor core internals. *Journal of Nuclear Materials*, 274(3):299–314, 1999.

[5] O.K. Chopra and A.S. Rao. Degradation of LWR core internal materials due to neutron irradiation, NUREG/CR-7027. 2010.

[6] G. S. Was, Y. Ashida, and P. L. Andresen. Irradiation-assisted stress corrosion cracking. 29(1-2):7–49, 2011.

[7] O.K. Chopra and A.S. Rao. A review of irradiation effects on lwr core internal materials – iascc susceptibility and crack growth rates of austenitic stainless steels. *Journal of Nuclear Materials*, 409(3):235–256, 2011.

[8] S. Lozano-Perez, J. Dohr, M. Meisnar, and K. Kruska. Scc in pwrs: Learning from a bottom-up approach. *Metallurgical and Materials Transactions E*, 1(2):194–210, Jun 2014.

[9] A. Hojná. Overview of intergranular fracture of neutron irradiated austenitic stainless steels. *Metals*, 7(10), 2017.

[10] G. S. Was and P. L. Andresen. 3 - mechanisms behind irradiation-assisted stress corrosion cracking. In Stefan Ritter, editor, *Nuclear Corrosion*, European Federation of Corrosion (EFC) Series, pages 47–88. Woodhead Publishing, 2020.

[11] F. Somville, R. Gérard, R.W. Bosch, and S. Gavrilov. Ageing management of baffle former bolts in belgian nuclear power plants. In *FONTEVRAUD 8 - Contribution of Materials Investigations & Operating Experience to LWR's Safety, Performance & Reliability*, sep 2014. Score = 3; FONTEVRAUD 8 - Contribution of Materials Investigations and Operating Experience to LWRs' Safety, Performance and Reliability ; Conference date: 15-09-2014 Through 18-09-2014.

[12] W. Karlsen, "The role of non-monotonic loading in EAC - a literature review," VTT Report, VTT-R-00867-12, Espoo, Finland, 2012.

[13] Z. Que, C. Huotilainen, T. Seppänen, J. Lydman, and U. Ehrnstén. Effect of machining on near surface microstructure and the observation of martensite at the fatigue crack tip in PWR environment of 304L stainless steel. *Journal of Nuclear Materials*, 558:153399, 2022.

[14] O. Chopra and G. Stevens, "Effect of LWR water environments on the fatigue life of reactor materials," (NUREG/CR-6909, Revision 1) –Final Report, 2018.

[15] R.W. Bosch, M. Vankeerberghen, R. Gérard, and F. Somville. Crack initiation testing of thimble tube material under pwr conditions to determine a stress threshold for iascc. *Journal of Nuclear Materials*, 461:112–121, 2015.

[16] M.J. Konstantinović. Internal oxidation and probabilistic fracture model of irradiation assisted stress corrosion cracking in stainless steels. *Journal of Nuclear Materials*, 495:220–224, 2017.

[17] P. M. Scott and M. Le Calver. *Some possible mechanisms of intergranular stress corrosion cracking of Alloy 600 in PWR primary water*. Minerals, Metals ampersand Materials Society, United States, 1993.

[18] P. M. Scott. An overview of internal oxidation as a possible explanation of intergranular stress corrosion cracking of alloy 600 in pwrs. pages 1–14, 1999.

[19] Lozano-Perez S., Mesisnar M., Dohr I., Kruska K., Reviewing the internal oxidation mechanism as a plausible explanation for SCC in PWR primary water, in: 16th International Conference on Environmental Degradation of Materials in Nuclear Power System—Water Reactors, 2013.

[20] A.G. Penders, M.J. Konstantinović, T. Yang, R. W. Bosch, D. Schryvers, and F. Somville. Microstructural investigation of iascc crack tips extracted from thimble tube o-ring specimens. *Journal of Nuclear Materials*, 565:153727, 2022.

[21] G. Kurdjumow and G. Sachs. Der mechanismus der stahlhã¤rtung. *Naturwissenschaften*, 18(22):534–534, May 1930.

[22] 2 - crystallography of martensite (general). In M. E. Fine, M. Meshii, C.M. Wayman, and Z. Nishiyama, editors, *Martensitic Transformation*, pages 14–134. Academic Press, 1978.

[23] K. Koumatos and A. Muehlemann. A theoretical investigation of orientation relationships and transformation strains in steels. *Acta Crystallographica Section A: Foundations and Advances*, 73:115–123, 2017.

[24] W. Karlsen, G. Diego, and B. Devrient. Localized deformation as a key precursor to initiation of intergranular stress corrosion cracking of austenitic stainless steels employed in nuclear power plants. *Journal of Nuclear Materials*, 406(1):138–151, 2010. FP6 IP PERFECT Project: Prediction of Irradiation Damage Effects in Reactor Components.

[25] D. R. Steinmetz, T. Jäpel, B. Wietbrock, P. Eisenlohr, I. Gutierrez-Urrutia, A. Saeed–Akbari, T. Hickel, F. Roters, and D. Raabe. Revealing the strain-hardening behavior of twinning-induced plasticity steels: Theory, simulations, experiments. *Acta Materialia*, 61(2):494–510, 2013.

[26] J Talonen, H. Hänninen, P. Nenonen, and G. Pape. Effect of strain rate on the strain-induced $\gamma \rightarrow \alpha$'-martensite transformation and mechanical properties of austenitic stainless steels. *Metallurgical and Materials Transactions A*, 36(2):421–432, Feb 2005.

[27] W. Van Renterghem, M.J. Konstantinović, and M. Vankeerberghen. Evolution of the radiation-induced defect structure in 316 type stainless steel after post-irradiation annealing. *Journal of Nuclear Materials*, 452(1):158–165, 2014.

[28] R.W. Bosch, M. Konstantinovic, M. Vankeerberghen, R. Gérard, and F. Somville. Effect of cyclic loading on iascc stress threshold of thimble tube material with a dose up to 80 dpa under pwr conditions. In *International Symposium Contribution of Materials Investigations and Operating Experience to Light Water NPPs' Safety, Performance and Reliability*, pages 1–11, sep 2018. 3; 2018 - FONTEVRAUD 9 ; Conference date: 17-09-2018 Through 20-09-2018.

[29] Technical report. Materials Reliability Program: Characterizations of Type 316 Cold Worked Stainless Steel Highly Irradiated Under PWR Operating Conditions (International IASCC Advisory Committee Phase 3 Program Interim Report) (MRP-202). EPRI, Palo Alto, CA: 2006. 1013418. 11303336.

[30] H. Nishioka, K. Fukuya, K. Fujii, and Y. Kitsunai. Deformation structure in highly irradiated stainless steels. *Journal of Nuclear Science and Technology*, 45(4):274–287, 2008.

[31] N. Hashimoto, S.J. Zinkle, A.F. Rowcliffe, J.P. Robertson, and S. Jitsukawa. Deformation mechanisms in 316 stainless steel irradiated at 60°c and 330°c. *Journal of Nuclear Materials*, 283-287:528–534, 2000. 9th Int. Conf. on Fusion Reactor Materials.

[32] P. B. Hirsch, A. Howie, R. B. Nicholson, D. W. Pashley, M. J. Whelan, and L. Marton. Electron microscopy of thin crystals. *Physics Today*, 19(10):93–95, 1966.

[33] M. Meisnar, A. Vilalta-Clemente, A. Gholinia, M. Moody, A. J. Wilkinson, N. Huin, and S. Lozano-Perez. Using transmission kikuchi diffraction to study intergranular stress corrosion cracking in type 316 stainless steels. *Micron*, 75:1–10, 2015.

[34] S. Lozano-Perez, T. Yamada, T. Terachi, M. Schröder, C.A. English, G.D.W. Smith, C.R.M. Grovenor, and B.L. Eyre. Multi-scale characterization of stress corrosion cracking of cold-worked stainless steels and the influence of cr content. *Acta Materialia*, 57(18):5361–5381, 2009.

[35] S. M. Bruemmer and L. E. Thomas. High-resolution characterizations of stress-corrosion cracks in austenitic stainless steel from crack growth tests in bwr-simulated environments.

[36] P. Deng, Q. Peng, E.H. Han, W. Ke, C. Sun, and Z. Jiao. Effect of irradiation on corrosion of 304 nuclear grade stainless steel in simulated pwr primary water. *Corrosion Science*, 127:91–100, 2017.

[37] T. Fukumura, K. Fukuya, K. Fujii, T. Miura, and Y. Kitsunai. Grain boundary oxidation of neutron irradiated stainless steels in simulated pwr water. In J. H. Jackson, D. Paraventi, and M. Wright, editors, *Proceedings of the 18th International Conference on Environmental Degradation of Materials in Nuclear Power Systems – Water Reactors*, pages 2153–2163, Cham, 2019. Springer International Publishing.

[38] S. Lozano-Perez, K. Kruska, I. Iyengar, T. Terachi, and T. Yamada. The role of cold work and applied stress on surface oxidation of 304 stainless steel. *Corrosion Science*, 56:78–85, 2012.

[39] G.B. Olson and M. Cohen. A mechanism for the strain-induced nucleation of martensitic transformations. *Journal of the Less Common Metals*, 28(1):107–118, 1972.

[40] G. Meric de Bellefon and J.C. van Duysen. Tailoring plasticity of austenitic stainless steels for nuclear applications: Review of mechanisms controlling plasticity of austenitic steels below 400 °c. *Journal of Nuclear Materials*, 475:168–191, 2016.

[41] G. Shirane, D.E. Cox, and S.J. Pickart. Magnetic structures in FeCr2S4 and FeCr2 O4. *J. Appl. Phys.*, 35(2):954—955, 1964.

[42] K. N. Subramanyam. Neutron and x-ray diffraction studies of certain doped nickel ferrites. *Journal of Physics C: Solid State Physics*, 4(15):2266–2268, oct 1971.

[43] L. Legras, M. Boisson, E. Fargeas, P. Cuvillier, R. Mercier, S. Miloudi, J. Tarabay, and M. Roch. Tem investigations of the microstructure and oxides at the tip of intergranular cracks of a baffle former bolt irradiated up to 10 dpa. In *International Symposium Contribution of Materials Investigations and Operating Experience to Light Water NPPs' Safety, Performance and Reliability*, pages 1–12, sep 2018. 3; 2018 - FONTEVRAUD 9 ; Conference date: 17-09-2018 Through 20-09-2018.

[44] D.J. Edwards, E.P. Simonen, F.A. Garner, L.R. Greenwood, B.M. Oliver, and S.M. Bruemmer. Influence of irradiation temperature and dose gradients on the microstructural evolution in neutron-irradiated 316ss. *Journal of Nuclear Materials*, 317(1):32–45, 2003.

[45] M. Koyama, E. Akiyama, K. Tsuzaki, and D. Raabe. Hydrogen-assisted failure in a twinning-induced plasticity steel studied under in situ hydrogen charging by electron channeling contrast imaging. *Acta Materialia*, 61(12):4607–4618, 2013.

[46] A. H. King. Diffusion induced grain boundary migration. *International Materials Reviews*, 32(1):173–189, 1987.

[47] H. Lopez. Role of dislocations and generation of twins during diffusion induced grain boundary migration. *Materials Science and Technology*, 7(8):681–685, 1991.

[48] Z. Jiao and G.S. Was. Localized deformation and iascc initiation in austenitic stainless steels. *Journal of Nuclear Materials*, 382(2):203–209, 2008. Microstructural Processes in Irradiated Materials.

[49] T. Onchi, K. Dohi, N. Soneda, J.R. Cowan, R.J. Scowen, and M.L Castaño. Fractographic and microstructural characterization of irradiated 304 stainless steel intergranularly fractured in inert gas. *Journal of Nuclear Materials*, 320(3):194–208, 2003.

[50] Rémy, L. The interaction between slip and twinning systems and the influence of twinning on the mechanical behavior of fcc metals and alloys. Metall Mater Trans A 12, 387–408 (1981).

[51] Y.H. Lu, Q.J. Peng, T. Sato, and T. Shoji. An atem study of oxidation behavior of scc crack tips in 304l stainless steel in high temperature oxygenated water. *Journal of Nuclear Materials*, 347(1):52–68, 2005.

[52] Z. Shen, D. Du, L. Zhang, and S. Lozano-Perez. An insight into pwr primary water scc mechanisms by comparing surface and crack oxidation. *Corrosion Science*, 148:213–227, 2019.

[53] T. Shoji, Z. Lu, and H. Murakami. Formulating stress corrosion cracking growth rates by combination of crack tip mechanics and crack tip oxidation kinetics. *Corrosion Science*, 52(3):769–779, 2010.

[54] H.E. Evans, H.Y. Li, and P. Bowen. A mechanism for stress-aided grain boundary oxidation ahead of cracks. *Scripta Materialia*, 69(2):179–182, 2013.

[55] J. L. Straalsund and J. F. Bates. Partial molar volumes and size factor data for alloy constituents of stainless steel. *Metallurgical and Materials Transactions B*, 5(2):493–498, Feb 1974.

[56] H. E. Evans. Stress effects in high temperature oxidation of metals. *International Materials Reviews*, 40(1):1–40, 1995.

[57] K. Fukuya, H. Nishioka, K. Fujii, and Kitsunai Y. Characterization of iascc crack tip in highly irradiated stainless steels. In *14th International Conference on Environmental Degradation of Materials in Nuclear Power Systems Water Reactors 2009*, pages 1248–1258, Virginia Beach, VA, 08 2009. Curran Associates, Inc.

[58] A. Herbelin, T. Couvant, L. Legras, D. Delafosse, and G. Ilbevare. Oxidation of austenitic stainless steels in PWR primary water. In Centre Francais de l'Anticorrosion (CEFRACOR), editor, *European Corrosion Congress 2009 (EUROCORR 2009)*, volume 3, pages 1592–1608, Nice, France, Sep 2010. Curran Associates, Inc. 57 Morehouse Lane Red Hook, NY 12571 USA.

[59] H. Dugdale, D. E.J. Armstrong, E. Tarleton, S. G. Roberts, and S. Lozano-Perez. How oxidized grain boundaries fail. *Acta Materialia*, 61(13):4707–4713, 2013.

[60] R. W. Bosch, M.J. Konstantinović, A.G. Penders, M. Vankeerberghen, and F. Somville. Iascc crack initiation testing of thimble tube material under pwr conditions: effect of oxide layer, stress and load form. pages 1–10, sep 2022. 2022 - FONTEVRAUD 10; Conference date: 19-09-2022 Through 22-09-2022; Avignon - France.

[61] *Statistical Treatment of Strength*, chapter 7, pages 119–150. John Wiley & Sons, Ltd, 2009.

[62] H. Nishioka, K. Fukuya, K. Fujii, and T. Torimaru. Iascc initiation in highly irradiated stainless steels under uniaxial constant load conditions. *Journal of Nuclear Science and Technology*, 45(10):1072–1077, 2008.

[63] V. Tsakiris and D. V. Edmonds. Martensite and deformation twinning in austenitic steels. *Materials Science and Engineering: A*, 273-275:430–436, 1999.

[64] L. Yongfeng, B. Fuming, Wenbin K., and Hongliang P. Deformation-induced martensitic transformation behavior in cold-rolled aisi304 stainless steels. *Materials and Manufacturing Processes*, 28(3):256–259, 2013.

[65] G. B. Olson and M. Cohen. Stress-assisted isothermal martensitic transformation: Application to trip steels. *Metallurgical Transactions A*, 13(11):1907–1914, Nov 1982.

[66] W. Karlsen, A. Toivonen, and P. Efsing. Baseline examinations and autoclave tests of 65 and 100 dpa flux thimble tube o-ring specimens. *Corrosion and Materials Degradation*, 2(2):248–273, 2021.

[67] Y. Murakami and S. Matsuoka. Effect of hydrogen on fatigue crack growth of metals. *Engineering Fracture Mechanics*, 77(11):1926–1940, 2010. International Conference on Crack Paths 2009.

[68] A.J. Bogers and W.G. Burgers. Partial dislocations on the 110 planes in

the b.c.c. lattice and the transition of the f.c.c. into the b.c.c. lattice. *Acta Metallurgica*, 12(2):255–261, 1964.

[69] Y.F. Shen, X.X. Li, X. Sun, Y.D. Wang, and L. Zuo. Twinning and martensite in a 304 austenitic stainless steel. *Materials Science and Engineering: A*, 552:514–522, 2012.

[70] L. Bracke, L. Kestens, and J. Penning. Transformation mechanism of -martensite in an austenitic fe–mn–c–n alloy. *Scripta Materialia*, 57(5):385–388, 2007.